

Lung-Net: A deep learning framework for lung tissue segmentation in three-dimensional thoracic CT images

Niloufar Delfan

Abstract— Segmentation of lung tissue in computed tomography (CT) images is a precursor to most pulmonary image analysis applications. Semantic segmentation methods using deep learning have exhibited top-tier performance in recent years. This paper presents a fully automatic method for identifying the lungs in three-dimensional (3D) pulmonary CT images, which we call it Lung-Net. We conjectured that a significant deeper network with inceptionV3 units can achieve a better feature representation of lung CT images without increasing the model complexity in terms of the number of trainable parameters. The method has three main advantages. First, a U-Net architecture with InceptionV3 blocks is developed to resolve the problem of performance degradation and parameter overload. Then, using information from consecutive slices, a new data structure is created to increase generalization potential, allowing more discriminating features to be extracted by making data representation as efficient as possible. Finally, the robustness of the proposed segmentation framework was quantitatively assessed using one public database to train and test the model (LUNA16) and two public databases (ISBI VESSEL12 challenge and CRPF dataset) only for testing the model; each database consists of 700, 23, and 40 CT images, respectively, that were acquired with a different scanner and protocol. Based on the experimental results, the proposed method achieved competitive results over the existing techniques with Dice coefficient of 99.7, 99.1, and 98.8 for LUNA16, VESSEL12, and CRPF datasets, respectively. For segmenting lung tissue in CT images, the proposed model is efficient in terms of time and parameters and outperforms other state-of-the-art methods. Additionally, this model is publicly accessible via a graphical user interface.

Index Terms— Index Terms— Deep learning, Lung tissue, Medical imaging, Semantic segmentation.

I. INTRODUCTION

LUNG tissue segmentation is a crucial step in quantitatively analyzing thoracic computed tomography (CT) images in computer-aided medical diagnostic systems. This initial step significantly impacts the performance of downstream analyses, such as the detection of abnormalities or classification of lung diseases like cancer. [1]. Automatic and accurate lung tissue segmentation is challenging due to several image characteristics, such as low contrast, dynamic range,

spatial resolution, noise, and artifacts. The lung structure is primarily made up of air, which looks dark on a CT scan. Most segmentation algorithms rely on this contrast between the lung tissue and surrounding tissues. The existing lung segmentation techniques can be categorized into three groups: basic methods, model-based methods, and deep learning methods. The first category comprises thresholding [2-4], edge detection [5], region growing [6], connected components and graph search [7], watershed [8] and their combination [9]. These algorithms separate the lungs from airway by employing a volumetric model and removing the trachea and bronchus. To fill holes and trim edges, morphological operations or other post-processing steps are applied [10].

The second category of techniques, model-based methods, have been recognized as some of the most successful lung segmentation methods [10]. They rely on a geometric or statistical atlas of the lung, which is constructed using a large number of thoracic scans. Active shape models [11-14] and atlas-based deformable models [15, 16] are some examples in which the model parameters are updated based on training images to maintain maximum compatibility with new input images. Therefore, local distortions in segmented images are less likely to occur due to the inherent knowledge provided to the model.

Deep learning architectures constitute the third category of lung segmentation methods and promise better performance compared to model-based ones. A lung segmentation approach was proposed in [17] by combining fully convolutional networks (FCNs) and fully connected conditional random fields (CRFs). Alom et al. [18] proposed a framework based on recurrent neural networks (RNN) and U-net [19] for medical image segmentation. This framework was then applied to lung tissue segmentation by Kadia et al. [20]. In [21], a residual neural network based on the U-net was proposed as an alternative to shallow networks to extract more discriminative feature representations. In [22], another residual neural network based on the U-net was proposed, which employed residual multi-kernel pooling (RMP) and dense atrous convolution (DAC) as its backbone.

While several studies on large datasets suggest that a deeper network can achieve a better performance in image classification and segmentation [23], computational efficiency and low parameter count are still important factors for real-time image segmentation. These considerations motivated us to

explore network architectures that efficiently extract robust discriminative features. We focus on factorized convolutions and aggressive regularization.

In this study, to extract robust discriminative features from input CT images, we employed the U-Net architecture and integrated it with GoogleNet modules [24], namely InceptionV3 [25] blocks in the encoder path. For an efficient information representation from CT images, a 2.5-dimensional processing protocol was adopted [26]. CT images display image information in three dimensions. As such, considering a few consecutive slices (i.e., 2.5-dimension) can be more informative than individual 2-d slices for a better tissue separation and damage diagnosis. We extensively evaluated our method using three public lung tissue segmentation datasets, and showed its superiority over state-of-the-art methods.

II. METHODOLOGY

A. Datasets

Three publicly available datasets were used in this study: LUNA16, CRPF and VESSEL12. Lung Nodule Analysis 2016 (LUNA16) dataset [27] is a subset of the LIDC dataset [28] which includes 878 subjects. The images in LUNA16 represent a set of diagnostic and cancer screening lung CT scans in which the suspected lesions are annotated. The image sizes range from $512 \times 512 \times 95$ to $512 \times 512 \times 733$ voxels of size $0.78 \times 0.78 \times 1.25$ mm³. The ground truth (GT) was generated using an automatic segmentation algorithm [29]. It encompasses the right and left lungs and trachea as distinct labels. CRPF data from VIA/I-ELCAP [30] contains 50 thoracic computed tomography scans, consisting of diagnostic and screening thoracic CTs. Ten CT images that appeared to be highly corrupted by noise were excluded from the analysis. The voxel size is $0.71 \times 0.71 \times 1.25$ mm³ and the image sizes range from $512 \times 512 \times 212$ to $512 \times 512 \times 288$ voxels. Two radiologists generated GTs for this study. The GT images only include the left and right lungs, not the trachea. VESSEL12 [31], was provided for the segmentation challenge that took place in 2012 to compare methods for (semi-)automatic segmentation of the vessels in the lungs from chest computed tomography scans taken from both healthy and diseased populations. There are scans of both healthy subjects and patients with a variety of respiratory diseases that affect the lungs in a way that makes segmentation difficult. The CT images acquired from 23 subjects are included along with their corresponding lung masks. Our algorithm was tested on all scans, ranging in size from $512 \times 512 \times 355$ to $512 \times 512 \times 543$ voxels. This dataset includes a diverse set of clinical images, such as high resolution, low resolution, standard dose, and angio-CT, which is a CT scan with intravenous contrast. Each of these images has its own scanning parameters and reconstruction kernel. A description of the method to generate the GT masks which are comprised of only the left and right lungs can be found in [31]. Our algorithm did not see this dataset in training, and we used it only for testing.

B. Preprocessing

Two stages of preprocessing were performed on our data before feeding them to the 2.5D data generator. As typical CT scans were calibrated using Hounsfield units (approximate

intensities are: bone: +1000, water: ~ 0 , and air: ~ -1000) preprocessing was performed by first assigning a -1000 HU value to all boundary pixels where pixels initially have HU values of -3000. In the second step, to remove irrelevant structures from the image and enhance the contrast, all pixel values greater than 400 were set to 400, and those less than -1000 were set to -1000. This enhanced the distinguishability of the lung tissue from its adjacent tissues. Fig. 1(a) and (b) illustrate the histogram of an image's slice from LUNA16 before and after preprocessing, respectively. Fig. 1(a) and (b) show an example of a raw image and its preprocessed version, respectively. As indicated in Fig. 1(b), the lung tissue is discernible from other tissues, and the structure of tissues remains intact.

C. 2.5-Dimensional data generation

After the preprocessing step, 2.5-dimensional images comprising $n-1$, n , and $n+1$ th slices were generated, to train the proposed network to segment the n th image slice. Inspired by [26], three different data configurations were generated by assigning $n-1$, n , and $n+1$ slices in different orders to the red, green, and blue network input channels, respectively (Fig. 1(c)). The RGB configuration is generated by assigning slices $n-1$, n , and $n+1$ to the red, green, and blue input channels, respectively (Fig. 1(c)). The BGR configuration is generated using the slices $n-1$, n , and $n+1$ as blue, green, and red channels, respectively (Fig. 1(c)). The grey scale configuration is generated by assigning the same slice n to all three channels (Fig. 1(c)). Slice n was discarded if slice $n-1$ or $n+1$ was outside the CT volume. All these three data structures had the same GT as the n th slice.

D. Network Architecture

The proposed network architecture for segmentation of lungs from thoracic CTs is shown in Fig. 1(d). It is mainly inspired from a U-Net convolutional neural network (CNN) architecture [19], and then the encoder architecture was modified. The U-Net architecture benefits from skip connections between its encoder and decoder parts which enables it to provide better segmentation accuracy than previous networks [32]. The main idea behind our proposed architecture is to employ transfer learning in autoencoder part of the network. A pre-trained GoogleNet network with the InceptionV3 [25] modules are used as the transferred model in this study. InceptionV3 provided better accuracy in the Imagenet image segmentation challenge compared to former networks such as VGG and Resnet while being more efficient in terms of parameters. We removed the fully connected (FC) layers from the InceptionV3 architecture to be able to adopt it in the encoder part, and the decoder layers were added afterward. InceptionV3 receives the images through three color channels as input. Therefore, our 2.5-dimensional data structure including three slices can be introduced as input to three color channels. Our decoder architecture is the same as that of the U-Net model with no changes. Therefore, unsampled layers were used for decoding. Then, we used skip connections to link the corresponding layers within the encoder and decoder. Segmentation was obtained by feeding the image to an encoder first. Each step was followed by the transfer of the resulting feature map to the corresponding

where N is the number of pixels in the input image slice. This function compares the predicted value of all pixels (p_i) in the network output to their desired binary values (y_i) in the labelled GT image. It indicates how far the prediction is from the desired value. For binary classification, (1) gives the exact definition of the logarithmic cost function. Since the logarithm of this value is negative, the result is negated. The Dice coefficient was used as a statistical metric to evaluate the performance of our segmentation algorithm compared to the GT provided by the expert segmentation:

$$\text{Dice} = \frac{2|S \cap G|}{|S| + |G|} \quad (2)$$

where S and G represent the predicted mask and GT, respectively. \cap indicates an intersection of two sets, and refers to elements that are common to both sets [33].

F. Network Development

The proposed network was trained and tested using LUNA16 via 10-fold cross-validation strategy. A single iteration used 90% of the data to train the network and the remaining 10% to test its performance. In each iteration, 10% of the training data were randomly selected as a validation set to fine-tune the hyperparameters, and prevent overfitting. The hyperparameters included the optimizer, learning rate, and batch size [34]. The final model was used to report the results on unseen data. An early stopping strategy was employed to prevent overfitting. Upon failure to improve the value of the loss function on the validation data for more than five epochs, the training process was stopped and the network with the lowest value of the loss function was saved. We used the Adam [35] optimizer via a dynamic learning rate approach with an initial rate of 0.001. The learning rate was reduced using plateau callback during the training. Once the model performance stagnated for some epochs, the callback automatically reduced the learning rate. The batch size was set to 2 and the number of training epochs was set to 50.

III. EXPERIMENTAL RESULTS

The LUNA16 dataset was used for training and testing, while VESSEL12 and CRPF data were only used to assess the proposed model's performance. To compare our results with those of our counterparts, we computed Dice coefficients in both 2D and 3D. The 2D Dice coefficient was computed for every slice, and its average was calculated for all slices in a volumetric CT image. It is noteworthy that the 2D Dice criterion was calculated solely for slices that contain lungs in their GT, the network output, or both. In other words, the 2D Dice criterion was not applied to slices that contain no lung region neither in their GT nor in their segmentation result. The 3D Dice criterion was computed based on 3D GT and 3D segmentation result which was obtained by concatenating segmented slices of each CT image. Table I indicates the average and standard deviation of 2D and 3D Dice indices which were provided by our InceptionV3 based U-Net architecture for all three datasets. As shown in Table I, there was not large variation between the network performance in

TABLE I
SEGMENTATION RESULTS USING LUNG-NET MODEL

	Total (RGB)	Total (Gray)
Luna 16		
Dice score (2D)	0.960	0.953
STD (2D)	0.010	0.013
Dice score (3D)	0.997	0.992
STD (3D)	0.002	0.003
Vessel 12		
Dice score (2D)	0.951	0.943
STD (2D)	0.005	0.006
Dice score (3D)	0.991	0.987
STD (3D)	0.002	0.003
CRPF		
Radiologist 1		
Dice score (2D)	0.944	0.939
STD (2D)	0.006	0.007
Dice score (3D)	0.989	0.987
STD (3D)	0.002	0.002
Radiologist 2		
Dice score (2D)	0.943	0.938
STD (2D)	0.006	0.007
Dice score (3D)	0.988	0.987
STD (3D)	0.003	0.002

different folds which demonstrates its generalization property. On the LUNA16 dataset, the average 2D and 3D Dice coefficients of 0.96 and 0.997 were achieved, respectively. For the VESSEL12 dataset, our model achieved the average 2D and 3D Dice coefficients of 0.951 and 0.991, respectively. The GT for the CRPF dataset was not available publicly, so two radiologists (M. Pak and O. Ghaemi) examined the images and provided two sets of masks as GT. The proposed model achieved the average 2D and 3D Dice coefficients of 0.944 and 0.989 with the masks provided by the first radiologist and 0.93 and 0.988 with the masks provided by the second radiologist, respectively.

We also used the gray structure (column 3 in Table I) to demonstrate the capability of the model to segment 2D data. In this mode, only one slice is considered for 2.5D data generation. The results are shown in Table I. Fig. 2. illustrates the results of lung segmentation obtained using our method. A sample of results from the LUNA16 dataset can be seen in the first row. From left to right, three slices from the base, middle and apex part of the lung are shown. In each slice, the blue, red and white regions correspond to TP, FP and FN. The second row in Fig. 2. shows the results on some slices in a CT image from VESSEL2 dataset. The third and fourth rows in Fig. 2 correspond to the segmentation results of an image from CRPF dataset when the GT provided by the first and second radiologist are used for evaluation, respectively. As illustrated, the lung regions were successfully segmented from the input CT images in spite of their fuzzy boundaries and irregular shapes. Although, our method proves to remain robust while encountering new and unknown datasets, one can notice a decline in the average Dice coefficients of VESSEL12 and CRPF datasets compared to LUNA16. This can be justified by the fact that in the Luna16 dataset, the GT contains three

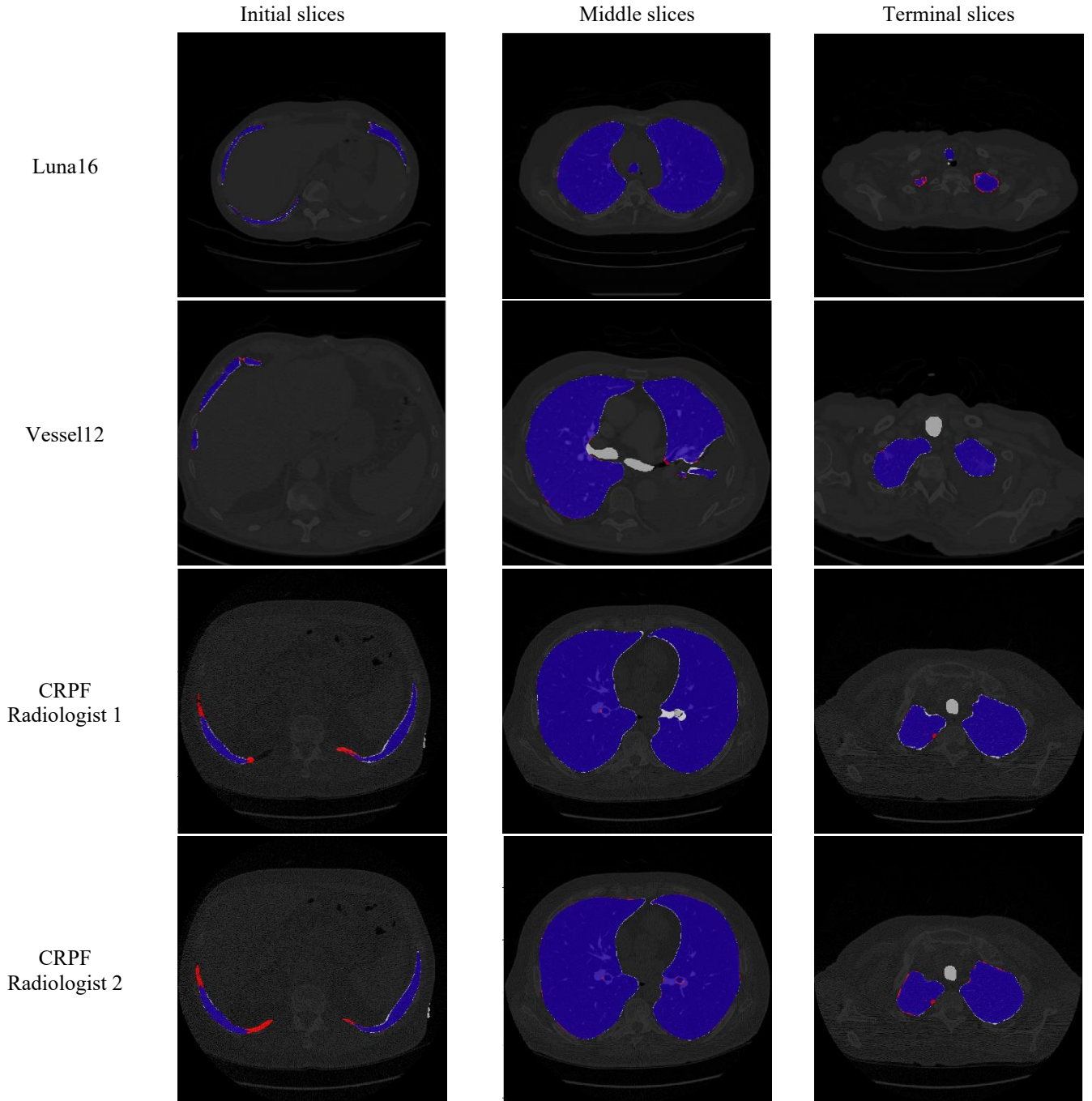


Fig. 2. The visual results of lung segmentation for all three datasets. blue color indicates the predicted lung region. False positive (FP) and false negative (FN) are indicated by red and white color respectively.

structures including left lung, right lung, and trachea, whereas in VESSEL12 and CRPF, it contains only left and right lungs. Fig. 3 shows a slice image from LUNA16 (left), its GT (middle) and the segmentation result which contains the trachea (right).

Table I also indicates that the 2D Dice score is generally inferior than 3D Dice score. This is partially due to the fact that 3D Dice score is the ratio between two volumes, while 2D Dice score is the average of the ratios between two areas in all slices of a CT image. Obviously, the decline in 2D Dice score due to small differences between two areas in all image slices is more pronounced than the decline in 3D Dice score due to a small

difference between two volumes. Furthermore, as the histograms of 2D Dice scores in Fig. 4. indicate, there are some zero score slices in each CT image. These zero Dice scores correspond to slices from extrem parts of the lung base and apex in which there exists no lung region either in GT or in the segmented image.

Table II, compares some existing methods from the literature with our proposed method for lung segmentation in thoracic CT scans. As indicated, the proposed method based on InceptionV3 outperformed all previous ones including conventional algorithms and deep neural networks. Additionally, it also

TABLE II
COMPARATIVE ANALYSIS OF THE PROPOSED METHOD WITH EXISTING WORKS.

Author	Data size	Validation method	Features	Segmentation technique	Performance evaluation
Private dataset					
Zhou et al. [36] 2016	240 scans	Custom split	Automated	FCN + majority voting	0.88
Zhou et al. [37] 2021	-	Custom split	Automated	Recurrent based on U-Net	0.992
Birbeck et al. [38] 2014	185 scans	Custom split	-	Statistical models +level set refinement	0.94
Sun et al. [12] 2011	30 scans	Custom split	-	Model based + Optimal surface finding	0.975
Gill et al. [13] 2014	190 scans	Custom split	3D scale-invariant	Model based	0.974
Xu et al. [39] 2019	201 scans	Custom split	K-means and CNN based	k-means & CNN	0.961
CRPF dataset					
Naseri et al. [16] 2018	40 scans	Leave-one-out	-	Model based	0.976
Proposed method	40 scans	Use only as test set	Automated	InceptionV3 -based U-net	0.988
Luna16 dataset					
Skourt et al. [40] 2018	All scans	Custom split	Automated	U-Net	0.950
Alom et al. [18] 2018	534 scans	Custom split	Automated	Recurrent network	0.98
Gu et al. [22] 2019	534 scans	Custom split	Automated	Residual U-Net + RMP + DAC	0.99
Khanna et al. [41] 2020	50 scans	5-fold cross-validation	Automated	Very deep Residual U-Net	0.986
Chen et al. [42] 2021	74 scans	Custom split	Automated	U-Net	0.974
Ma et al. [43] 2022	534 scans	Custom split	Automated	Context-attention network	0.989
Proposed method	879 scans	10-fold cross-validation	Automated	InceptionV3 -based U-net	0.997
Vessel12 dataset					
Alves et al. [17] 2018	20 scans	5-fold cross validation	Automated	FCN	0.991
Khanna et al. [41] 2020	20 scans	5-fold cross-validation	Automated	Very deep Residual U-Net	0.996
Soliman et al. [44] 2016	20 scans	Custom split	-	Markov-Gibbs random field	0.990
Chae et al. [45] 2016	-	Custom split	Geometric	Level set method	0.98
Proposed method	23 scans	Use only as test set	Automated	InceptionV3 -based U-net	0.991

illustrates that different cross-validation techniques are used to analyze the model performance. We differ from previous approaches in that we utilize the full units, which provides additional feature extraction power while maintaining the same number of parameters. Table II categorizes some lung segmentation methods based on their training and testing datasets. Previous approaches often used handcrafted features [2, 44, 45], model-based methods [1, 9, 13, 16, 44], shallow networks [17, 31, 36, 39, 40] or even more complicated end-to-

end CNN models [41] than ours. These methods produce robust discriminative features for semantic lung segmentation. Most of the methods that mentioned in Table II are usually trained and tested on the same dataset, so their performance on other datasets is unknown and highly dependent on the specific characteristics of the primary dataset. Model-based methods [12, 13, 16] require a large amount of training samples to be representative of the target population, so any lung shape not experienced by the model needs to be added to the learning set.

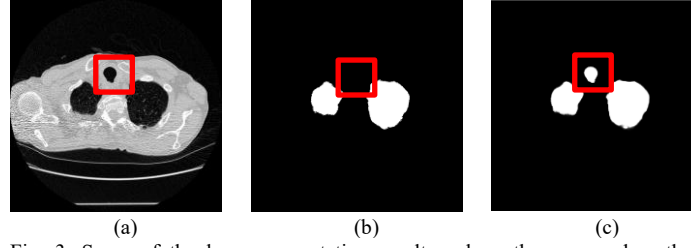


Fig. 3. Some of the lung segmentation results, where the proposed method segmented the trachea. The red box indicates: (a) trachea in the input image. (b) trachea in the GT. (c) trachea in the output.

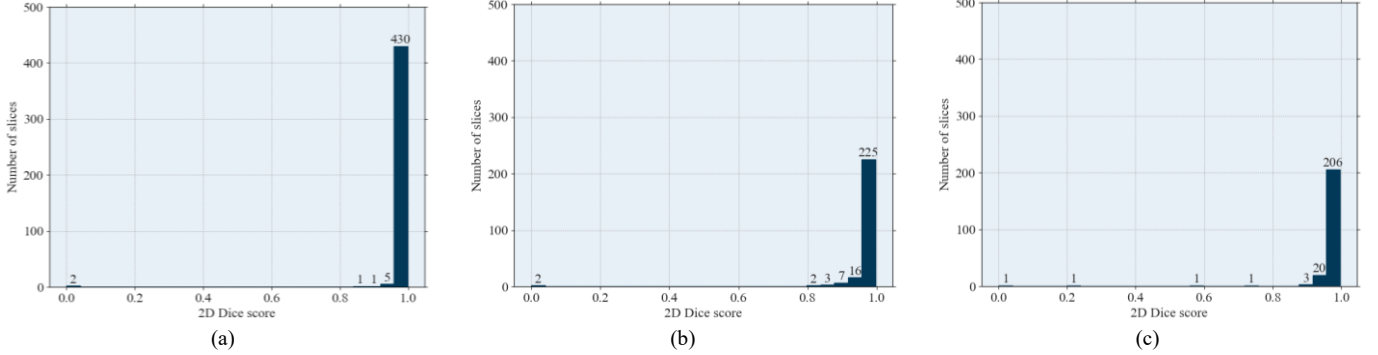


Fig. 4. The 2D dice coefficient distribution histograms for a CT image from (a) Luna16 dataset. (b) CRPF dataset. (c) VESSEL12 dataset.

TABLE III
EFFECT OF EACH DATA STRUCTURE SEPARATELY ON THE OVERALL PERFORMANCE ON THE LUNA16 DATASET.

	3D Dice score	STD
Concatenate	0.972	0.004
RGB	0.985	0.003
BGR	0.979	0.004

Left and right lungs are segmented separately in some methods [12, 38] which can result in inconsistencies (e.g., overlap). Alves et al. [17] did report a Dice score of 99.0 for the Vessel12 dataset, but the shallow network in their model prevented the extraction of complex features for pixel-wise classification. In addition, some authors [18, 22, 36, 37, 39, 43] have used a custom train test split method for cross validation, which could result in biased results for different distributions of data. In [41], only 50 subjects from the entire dataset were used for train, validate and test the model without specifying the selection criterion. Additionally, most of the existing methods [16, 36, 37, 41] reduced the resolution to 256*256 or 128*128, which may result in the generation of artifacts or even loss of important information in the images. The proposed method by Soliman et al. [44] achieved an outstanding accuracy, but these complex pipelines are not easily reproducible unless the source code and underlying atlases are shared. Our proposed method achieved enhanced performance compared to previous approaches as reported in Table II. Unlike previous approaches, our method was extensively validated using a 10-fold cross-

validation procedure, as well as deeper. on two additional datasets to guarantee its accuracy and robustness against new unseen data. The proposed model has 21,787,552 parameters which this value is about 25,583,592 for [41].

The performance results of the proposed model on the Luna16 dataset using each 2.5D data structure separately are shown in Table III. These 3D Dice scores are slightly less than the results obtained with three structures all together, as shown in Table I.

TABLE IV
COMPARATIVE ANALYSIS BETWEEN PROPOSED AND OTHER CNN MODULES

Model	3D Dice score	STD
FCN [46]	0.947	0.004
Basic U-net [19]	0.957	0.004
U-net+VGG16[47]	0.968	0.004
U-net+VGG19[47]	0.970	0.004
U-net+Resnet101[23]	0.973	0.004
U-net+Resnet34 [23]	0.978	0.003
U-net+DenseNet [48]	0.983	0.003
U-net+InceptionResnet V2 [49]	0.991	0.003
U-net+InceptionV3 [25]	0.997	0.002

A comparative analysis was carried out between our implemented model and various other CNN modules instead of InceptionV3 for semantic segmentation, as shown in Table IV. Our proposed model has also been compared with state-of-the-art segmentation methods, including FCN [46], U-Net [19], and a modified version of U-Net. The Luna16 dataset with similar training and testing strategies have been used for all of these networks. As indicated in Table V, the FCN model achieved the lowest performance in terms of Dice score. In compare with other models, FCN has a very shallow architecture, which justifies its low performance. Furthermore, the U-Net architecture has performed better than the FCN model with a Dice score of 95.7. Accordingly, we conclude that the U-Net model is a better candidate for lung segmentation. Nevertheless, the performance degradation problem becomes apparent as the network becomes deeper.

IV. CONCLUSION

In this work, we proposed a fully automated framework based on a deep convolutional neural network for lung CT segmentation. The implemented network leveraged the strength of both InceptionV3 and U-Net architecture. First, a deep InceptionV3-based U-Net was implemented for the semantic segmentation task. Second, a new data structure was utilized to enhance the generalization and feature extraction capability of the proposed method. The experiment results demonstrated that the proposed method is quite robust and segments the lung regions more precisely, even in the most complex lung images as compared to other methods. Our approach obtained competitive results when evaluated on three publicly available benchmark datasets namely, LUNA16, VESSEL12, and CRPF.

REFERENCES

- Armato III, S.G. and W.F. Sensakovic, *Automated lung segmentation for thoracic CT: impact on computer-aided diagnosis*. Academic Radiology, 2004. **11**(9): p. 1011-1021.
- Hu, S., E.A. Hoffman, and J.M. Reinhardt, *Automatic lung segmentation for accurate quantitation of volumetric X-ray CT images*. IEEE transactions on medical imaging, 2001. **20**(6): p. 490-498.
- Mardia, K.V. and T. Hainsworth, *A spatial thresholding method for image segmentation*. IEEE transactions on pattern analysis and machine intelligence, 1988. **10**(6): p. 919-927.
- Karthikeyan, A. and M. Valliammai, *Lungs segmentation using multi-level thresholding in CT images*. Int. J. Electron. Comput. Sci. Eng, 2012. **1**: p. 1509-1513.
- PhD, D.C., *Global and segmented search for lung nodules of different edge gradients*. Investigative Radiology, 1980. **15**(3).
- Dehmeshki, J., et al., *Segmentation of pulmonary nodules in thoracic CT scans: a region growing approach*. IEEE transactions on medical imaging, 2008. **27**(4): p. 467-480.
- Felzenszwalb, P.F. and D.P. Huttenlocher, *Efficient graph-based image segmentation*. International journal of computer vision, 2004. **59**(2): p. 167-181.
- Shojaii, R., J. Alirezaie, and P. Babyn. *Automatic lung segmentation in CT images using watershed transform*. in *IEEE international conference on image processing 2005*. 2005. IEEE.
- Garnavi, R., et al. *A new segmentation method for lung HRCT images*. in *Digital Image Computing: Techniques and Applications (DICTA'05)*. 2005. IEEE.
- Sluimer, I., et al., *Computer analysis of computed tomography scans of the lung: a survey*. IEEE transactions on medical imaging, 2006. **25**(4): p. 385-405.
- Kass, M., A. Witkin, and D. Terzopoulos, *Snakes: Active contour models*. International journal of computer vision, 1988. **1**(4): p. 321-331.
- Sun, S., C. Bauer, and R. Beichel, *Automated 3-D segmentation of lungs with lung cancer in CT data using a novel robust active shape model approach*. IEEE transactions on medical imaging, 2011. **31**(2): p. 449-460.
- Gill, G., M. Toews, and R.R. Beichel, *Robust initialization of active shape models for lung segmentation in CT scans: A feature-based atlas approach*. International journal of biomedical imaging, 2014. **2014**.
- Cootes, T.F., et al., *Active shape models-their training and application*. Computer vision and image understanding, 1995. **61**(1): p. 38-59.
- Iglesias, J.E. and M.R. Sabuncu, *Multi-atlas segmentation of biomedical images: a survey*. Medical image analysis, 2015. **24**(1): p. 205-219.
- Naseri Samaghcheh, Z., et al., *A new model-based framework for lung tissue segmentation in three-dimensional thoracic CT images*. Signal, Image and Video Processing, 2018. **12**(2): p. 339-346.
- Alves, J.H., P.M.M. Neto, and L.F. Oliveira. *Extracting lungs from CT images using fully convolutional networks*. in *2018 International joint conference on neural networks (IJCNN)*. 2018. IEEE.
- Alom, M.Z., et al., *Recurrent residual convolutional neural network based on u-net (r2u-net) for medical image segmentation*. arXiv preprint arXiv:1802.06955, 2018.
- Ronneberger, O., P. Fischer, and T. Brox. *U-net: Convolutional networks for biomedical image segmentation*. in *International Conference on Medical image computing and computer-assisted intervention*. 2015. Springer.
- Kadia, D.D., et al., *R 2 U3D: Recurrent Residual 3D U-Net for Lung Segmentation*. IEEE Access, 2021. **9**: p. 88835-88843.
- Korkalainen, H., et al., *Accurate deep learning-based sleep staging in a clinical population with suspected obstructive sleep apnea*. IEEE journal of biomedical and health informatics, 2019. **24**(7): p. 2073-2081.
- Gu, Z., et al., *Ce-net: Context encoder network for 2d medical image segmentation*. IEEE transactions on medical imaging, 2019. **38**(10): p. 2281-2292.
- He, K., et al. *Deep residual learning for image recognition*. in *Proceedings of the IEEE conference on computer vision and pattern recognition*. 2016.
- Szegedy, C., et al. *Going deeper with convolutions*. in *Proceedings of the IEEE conference on computer vision and pattern recognition*. 2015.
- Szegedy, C., et al. *Rethinking the inception architecture for computer vision*. in *Proceedings of the IEEE conference on computer vision and pattern recognition*. 2016.
- Xu, Y., T. Géraud, and I. Bloch. *From neonatal to adult brain MR image segmentation in a few seconds using 3D-like fully convolutional network and transfer learning*. in *2017 IEEE International Conference on Image Processing (ICIP)*. 2017. IEEE.
- Setio, A.A.A., et al., *Validation, comparison, and combination of algorithms for automatic detection of pulmonary nodules in computed tomography images: the LUNA16 challenge*. Medical image analysis, 2017. **42**: p. 1-13.
- Armato III, S.G., et al., *The lung image database consortium (LIDC) and image database resource initiative (IDRI): a completed reference database of lung nodules on CT scans*. Medical physics, 2011. **38**(2): p. 915-931.
- van Rikxoort, E.M., et al., *Automatic lung segmentation from thoracic computed tomography scans using a hybrid approach with error detection*. Medical physics, 2009. **36**(7): p. 2934-2947.
- Reeves, A.P., et al. *A public image database to support research in computer aided diagnosis*. in *2009 Annual International Conference of the IEEE Engineering in Medicine and Biology Society*. 2009. IEEE.
- Rudyanto, R.D., et al., *Comparing algorithms for automated vessel segmentation in computed tomography scans of the lung: the VESSEL12 study*. Medical image analysis, 2014. **18**(7): p. 1217-1232.
- Drozdal, M., et al., *The importance of skip connections in biomedical image segmentation*, in *Deep learning and data labeling for medical applications*. 2016, Springer. p. 179-187.

33. Sonka, M., V. Hlavac, and R. Boyle, *Image processing, analysis, and machine vision*. 2014: Cengage Learning.
34. Bengio, Y., *Practical recommendations for gradient-based training of deep architectures*, in *Neural networks: Tricks of the trade*. 2012, Springer. p. 437-478.
35. Kingma, D.P. and J. Ba, *Adam: A method for stochastic optimization*. arXiv preprint arXiv:1412.6980, 2014.
36. Zhou, X., et al., *Three-dimensional CT image segmentation by combining 2D fully convolutional network with 3D majority voting*, in *Deep Learning and Data Labeling for Medical Applications*. 2016, Springer. p. 111-120.
37. Zhou, L., et al. *LTS-NET: Lung Tissue Segmentation from CT Images using Fully Convolutional Neural Network*. in *2021 11th International Conference on Information Science and Technology (ICIST)*. 2021. IEEE.
38. Birkbeck, N., et al. *Lung segmentation from CT with severe pathologies using anatomical constraints*. in *International conference on medical image computing and computer-assisted intervention*. 2014. Springer.
39. Xu, M., et al., *Segmentation of lung parenchyma in CT images using CNN trained with the clustering algorithm generated dataset*. Biomedical engineering online, 2019. **18**(1): p. 1-21.
40. Skourt, B.A., A. El Hassani, and A. Majda, *Lung CT image segmentation using deep neural networks*. Procedia Computer Science, 2018. **127**: p. 109-113.
41. Khanna, A., et al., *A deep Residual U-Net convolutional neural network for automated lung segmentation in computed tomography images*. Biocybernetics and Biomedical Engineering, 2020. **40**(3): p. 1314-1327.
42. Chen, K.-b., et al., *Lung computed tomography image segmentation based on U-Net network fused with dilated convolution*. Computer Methods and Programs in Biomedicine, 2021. **207**: p. 106170.
43. Ma, M., et al., *HT-Net: hierarchical context-attention transformer network for medical ct image segmentation*. Applied Intelligence, 2022: p. 1-14.
44. Soliman, A., et al., *Accurate lungs segmentation on CT chest images by adaptive appearance-guided shape modeling*. IEEE transactions on medical imaging, 2016. **36**(1): p. 263-276.
45. Chae, S.-H., et al., *Automatic lung segmentation for large-scale medical image management*. Multimedia Tools and Applications, 2016. **75**(23): p. 15347-15363.
46. Long, J., E. Shelhamer, and T. Darrell. *Fully convolutional networks for semantic segmentation*. in *Proceedings of the IEEE conference on computer vision and pattern recognition*. 2015.
47. Simonyan, K. and A. Zisserman, *Very deep convolutional networks for large-scale image recognition*. arXiv preprint arXiv:1409.1556, 2014.
48. Huang, G., et al. *Densely connected convolutional networks*. in *Proceedings of the IEEE conference on computer vision and pattern recognition*. 2017.
49. Szegedy, C., et al. *Inception-v4, inception-resnet and the impact of residual connections on learning*. in *Thirty-first AAAI conference on artificial intelligence*. 2017.